Continuum Mech. Thermodyn. (2019) 31:703–713
https://doi.org/10.1007/s00161-018-0721-z

ORIGINAL ARTICLE

Tim Fischer · Ewald Werner · Sonun Ulan kyzy · Oliver Munz

Crystal plasticity modeling of polycrystalline Ni-base superalloy honeycombs under combined thermo-mechanical loading

Received: 27 July 2018 / Accepted: 29 September 2018 / Published online: 13 October 2018

Abstract To meet the ever-growing demands for the efficient operation of turbomachinery, a minimum clearance between the rotating and the stationary components is of great importance. A lack of controlling this clearance often leads to interface rubbing. As a result, thermo-mechanical loads arise that can critically damage both components. Maintaining operational reliability and high efficiency requires seal systems that can tolerate rubbing. Honeycomb labyrinth seals can fulfill this task. In this contribution, we present a three-dimensional microstructure-based simulation approach considering the periodic unit cell of a polycrystalline Ni-base superalloy (Hastelloy X) honeycomb structure. Different honeycomb geometries are investigated, and various loading conditions are applied to simulate the thermo-mechanical behavior of the honeycomb structure during rubbing. The problem is solved in a finite element framework, and the deformation behavior is described by a crystal plasticity model accounting for microstructure attributes of the material. To calibrate the material model, numerical simulations on a representative volume element discretized with a realistic three-dimensional periodic mesh are carried out. The overall thermo-mechanical response of the honeycomb structure as well as the development of local field quantities is investigated. The study reveals that large contact areas seem to be very critical for the initiation of premature damage of the honeycomb structure.

Keywords Honeycombs · Crystal plasticity · Ni-base superalloy · Thermo-mechanical analysis

1 Introduction

Rubbing is a near-surface phenomenon that takes place when the rotating and the stationary components of a gas turbine engine contact each other. Since only a very small clearance between the components is desired for an efficient operation, rubbing cannot always be avoided. Thus, combined thermo-mechanical loads occur and can critically damage both components. To ensure operational reliability and high efficiency, rubbing-tolerant honeycomb structures are used on the stationary side of the seal system (Fig. 1). These honeycomb structures combine low weight with a substantial out-of-plane shear stiffness and strength [28–30,47]. The cell wall

Communicated by Andreas Öchsner.

T. Fischer (✉) · E. Werner
Institute of Material Science and Mechanics of Materials, Technische Universität München, Boltzmannstraße 15, 85748 Garching, Germany
E-mail: fischer@wkm.mw.tum.de

S. Ulan kyzy
Metals and Alloys, Universität Bayreuth, Ludwig-Thoma-Straße 36b, 95447 Bayreuth, Germany

O. Munz
Institute of Thermal Turbomachinery, Karlsruher Institut für Technologie, Kaiserstraße 12, 76131 Karlsruhe, Germany

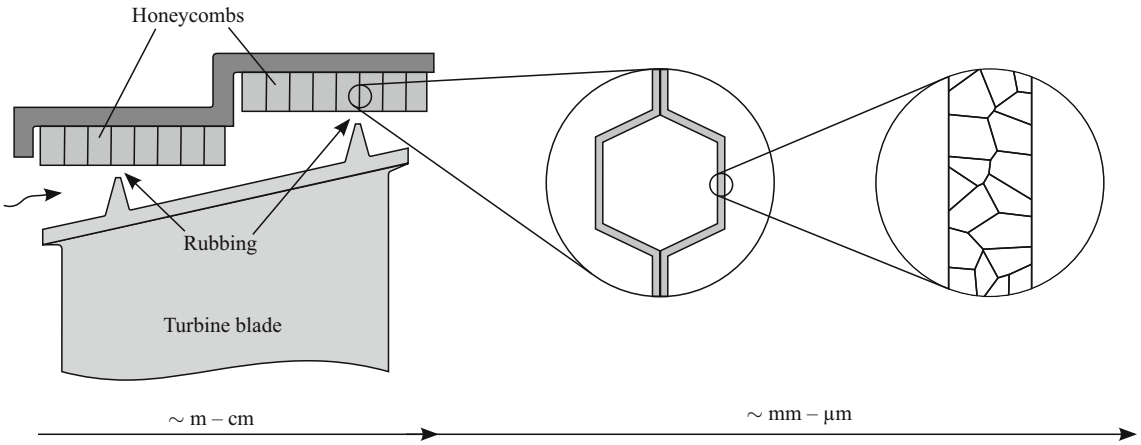

Fig. 1 Schematic representation of a seal system in a gas turbine with a detailed view of the polycrystalline Ni-base superalloy honeycomb structure

thickness of the honeycomb structures is only a few micrometers. Hence, the size of the deformation/damage fields of the honeycomb structures has the same characteristic length as microstructure features of the material.

Ni-base superalloys are used as material for the stationary component due to their capability of withstanding high thermo-mechanical loads. Polycrystalline Hastelloy X is one of the most widely used materials for metallic honeycomb structures. This single γ-phase Ni-base superalloy with a face-centered cubic (fcc) lattice structure is particle strengthened by very fine carbides and has a relatively low strength but high ductility at elevated temperatures [43]. The material has been well characterized in the past [2,3,6,19,21,40,43].

Conventional smeared-out material models (J_2 plasticity) are suitable to describe the macroscopic behavior of the inhomogeneous material. However, these material models fail to capture the influence of microstructure attributes such as crystal orientation, grain size or grain size distribution on the mechanical behavior. Constitutive relations based on the crystal plasticity theory can explicitly describe such effects of the microstructure and have been applied in the past for a wide variety of materials and loading scenarios [37]. Two-dimensional and three-dimensional crystal plasticity models have been recently developed for polycrystalline Ni-base superalloys [4,9,13,14,22,24,25,31,32,34,41,42,44,49,52,53]. Most of these studies focus on the thermo-mechanical fatigue behavior. Very capable crystal plasticity modeling approaches were developed by McDowell and coworkers [8,15–18,50,51] . They set up a microstructure-sensitive model to study the influence of the microstructure on fretting, which is similar to rubbing a near-surface phenomenon. Their results showed, that the average grain size has a considerable influence on the plastic deformation and the fretting fatigue behavior of the titanium alloy Ti-6Al-4V. The finite element model for the fretting fatigue simulations consists of a so-called embedded cell approach [5,48] in which small regions of special interest (e.g., near-surface regions in case of fretting or rubbing) are resolved with a discrete microstructure, while the remainder of the structure is approximated by the macroscopic smeared-out material model (J_2 plasticity). As a result, local stress and strain fields of particular interest can be studied at high detail in a computationally efficient way.

Within this contribution, we present fully three-dimensional rubbing simulations for a polycrystalline Hastelloy X honeycomb structure. The deformation behavior of the material is described within a crystal plasticity framework based on the work of Meier et al. [26,27,48] (Sect. 2). The crystal plasticity model parameters are calibrated by simulation of representative volume elements (RVEs) [5,10,45,48]. In Sect. 3, the finite element model of the honeycomb structure based on the embedded cell approach is presented. The rubbing simulation results are discussed in Sect. 4. The sensitivity of the rubbing behavior to different loading conditions, different realizations of the microstructure and the geometry of the honeycomb structure is investigated. Section 5 concludes our contribution.

2 Constitutive model for the Ni-base superalloy

The constitutive relations of the crystal plasticity model can be found in detail in Meier et al. [26,27,48]. Effects of thermal expansion and temperature-dependent material behavior are taken into account in the model and are necessary for an accurate rubbing simulation. However, due to the extreme rubbing conditions, it is

Table 1 Summary of the elastic constants parameter according to Eq. (2) for the polycrystalline Hastelloy X [6,46]

Elastic constant	c_0, GPa	s, GPa	T_{ref}, °C
C_{11}	230.90	1.10	22.50
C_{12}	156.12	0.95	44.50
C_{44}	121.77	0.95	22.00

required to enrich the model by further temperature dependencies. The constitutive model is implemented into the finite element code ABAQUS/Standard using the user-material subroutine interface and the simulation toolkit DAMASK [7,36–38].

2.1 Crystal plasticity material model

As stress–strain relationship for the isotropic elastic material behavior, we employ Hooke's law:

$$\mathbf{S} = \mathbb{C} : \mathbf{E}, \tag{1}$$

where $\mathbf{S}$ is the second Piola–Kirchhoff stress, $\mathbb{C}$ the stiffness tensor and $\mathbf{E} = 1/2\left(\mathbf{F}_{\text{e}}^{\text{T}}\mathbf{F}_{\text{e}} - \mathbf{I}\right)$ the elastic Green–Lagrange strain calculated from the elastic deformation gradient $\mathbf{F}_{\text{e}}$. The dependence of the elastic stiffness constants C_{11}, C_{12} and C_{44} on temperature T is captured by the following relation [46]:

$$C = c_0 - \frac{s}{\exp\left(\frac{T_{\text{ref}}}{T}\right) - 1}, \tag{2}$$

in which c_0, s and T_{ref} are fitting constants. These constants have to be found for each of the three elastic stiffness constants separately. Table 1 lists the fitted constants for Hastelloy X. According to Schmid's law, the resolved shear stress τ^i acting on each slip system i depends on the slip direction $\mathbf{m}^i$, the slip plane normal $\mathbf{n}^i$ and the second Piola–Kirchhoff stress:

$$\tau^i = \mathbf{S} \cdot \left(\mathbf{m}^i \otimes \mathbf{n}^i\right). \tag{3}$$

A wide range of flow rules have been proposed to model the shear rate $\dot{\gamma}^i$ on a given slip system at elevated temperatures. In our case, the classical phenomenological power law description is enriched by an Arrhenius term:

$$\dot{\gamma}^i(T) = \dot{\gamma}_0 \exp\left(-\frac{Q_0}{RT}\right)\left|\frac{\tau^i - \chi^i}{\tau_{\text{c}}^i(T)}\right|^m \operatorname{sgn}\left(\tau^i - \chi^i\right). \tag{4}$$

The Arrhenius term is a function of the reference shear rate $\dot{\gamma}_0$, the energy of activation Q_0 for crystallographic slip of lattice dislocations and the universal gas constant R. The power law term comprises the resolved shear stress, a temperature-dependent critical resolved shear stress τ_{c}^i on each slip system, a back stress χ^i acting on a given slip system and the rate sensitivity of slip m. The critical resolved shear stress for all twelve slip systems of the fcc lattice is:

$$\dot{\tau}_{\text{c}}^i(T) = \sum_{j=1}^{12} q_{ij}\left[h_0\left(1 - \frac{\tau_{\text{c}}^j(T)}{\tau_{\text{s}}\Pi(T)}\right)^a\right] \cdot \left|\dot{\gamma}^j(T)\right|. \tag{5}$$

In this equation, the matrix q_{ij} is responsible for the latent hardening behavior between two different slip systems i and j, h_0 and a are slip hardening parameters and τ_{s} controls the saturation of the shear stress. The critical resolved shear stress as well as the saturation shear stress is scaled according to the Hall–Petch relationship and thereby accounting for the grain size effect:

$$\tau_{\text{c/s}} = \tau_{\text{c/s},0} + \frac{K_{\text{c/s}}}{\sqrt{d}}. \tag{6}$$

Table 2 Summary of the softening parameter $\Pi(T) \in [0, 1]$ determined from the yield strength of the polycrystalline Hastelloy X [19]

	20 °C	538 °C	649 °C	760 °C	871 °C	982 °C	1093 °C	1200 °C
$\Pi(T)$	1.000	0.646	0.644	0.625	0.512	0.240	0.113	0.053

$\tau_{c/s,0}$ and $K_{c/s}$ are material parameter and d is the grain size. In our work, grain size is defined as the diameter of a sphere of equivalent volume [35]. The temperature-dependent softening parameter $\Pi(T) \in [0, 1]$ in Eq. (5) has a significant influence on the material behavior. According to the actual temperature, the softening parameter adjusts the values for the critical resolved shear stress and the saturation stress. The softening parameter is determined from macroscopic quantities (e.g., yield strength or ultimate tensile strength) for a wide range of temperatures (Table 2) [19]. The rate of the back stress $\dot{\chi}^i$ on each slip system evolves from the nonlinear kinematic hardening rule of the Armstrong–Frederick type [11,20]:

$$\dot{\chi}^i = h\dot{\gamma}^i - r\chi^i \left|\dot{\gamma}^i\right|, \tag{7}$$

where h and r are coefficients for the hardening and dynamic recovery, respectively. Throughout our simulations, the initial back stress χ_0 on each slip system and both coefficients are set to zero ($h = r = \chi_0 = 0$), thus kinematic hardening is neglected.

2.2 Identification of the crystal plasticity material model parameters

The crystal plasticity model parameters are determined by simulation of three-dimensional virtual microstructures generated by Voronoï tessellation [39]. For this purpose, a method for the generation of three-dimensional periodic unstructured meshes is developed. Special attention is paid to the geometric periodicity of the grain structure in order to subject the micromechanical volume element to favorable periodic boundary conditions (PBCs) [23]. Figure 2, left, illustrates the two-dimensional periodic continuation of grains in space $\mathscr{X}$ of a unit cell with boundary $\Gamma_{\mathscr{X}}$. This can be achieved by duplicating each seed point p_i of a grain 26 times in all coordinate directions (three-dimensional tessellation) around the inner unit cell [10,12,33]. Additionally, a minimum distance $d_{\min}$ is assumed between all seed points $\left(\left|\left|p_i - p_j\right|\right|_2 \geq d_{\min}/2\right)$. By this, the number of small edges is significantly reduced and a smoother mesh generation is ensured. An example of the more complex but also more suitable three-dimensional (periodic) Voronoï tessellation with 150 grains is shown in Fig. 2, right. One main advantage of the presented method is that standard implementations of PBCs can be used, since a congruent mesh on the opposing faces of the volume element is generated automatically. The unstructured boundary finite element mesh of a volume element consisting only of tetrahedral elements with quadratic basis functions (denoted as C3D10) is shown in Fig. 3. The unstructured mesh approach ensures an exact resolution of the grain boundaries and the local field quantities. In our studies, the assignment of the crystallographic orientation to the individual grains is based on an algorithm for a fully random orientation distribution (random texture).

In order to achieve representative results for the micromechanical volume element, a convergence study is conducted. The convergence study employs volume elements with different numbers of grains and finite element mesh densities. Figure 4, left, summarizes the results of this study. For each simulation, the volume element is loaded with a volume-averaged normal strain $< \varepsilon_{33} >= 10\ \%$ and the resulting volume-averaged normal stress $< \sigma_{33} >$ is normalized by the maximum volume-averaged normal stress $< \sigma_{33}^{\max} >$. To control the total deformation of the volume element, the displacement degrees of freedom on the outside of the cube are coupled with a total of three reference nodes. Displacements can then be applied to these reference nodes for mechanically loading. Due to the random assignment of the crystallographic orientation to the individual grains, five calculations with varying orientation distribution of the grains are performed for each microstructural realization (with the exception of the unit cell consisting of 350 grains due to the extreme computational effort and the fact that this large number of grains diminishes the variability due to the random assignment of the specific orientations to the individual grains). Subsequently, the arithmetic mean and the standard deviation are determined. On the basis of four different microstructural realizations (20, 100, 150 and 350 grains), we found that a volume element with 150 grains is sufficiently large to yield representative results. A similar minimum number of grains can be found in the literature for both crystal plasticity and conventional

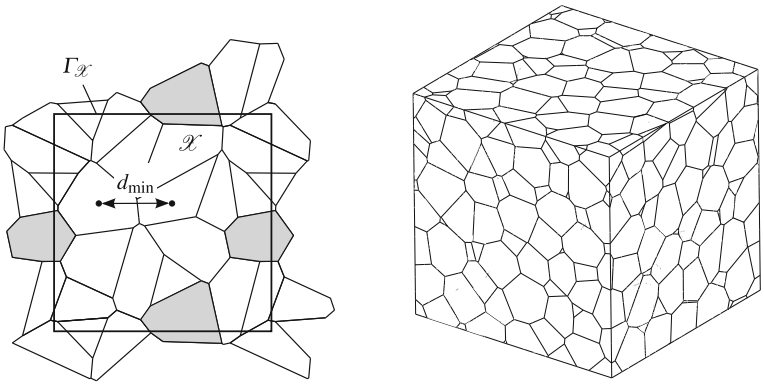

Fig. 2 Two-dimensional (periodic) Voronoï tessellation in space $\mathscr{X}$ of a unit cell with boundary $\Gamma_{\mathscr{X}}$ (*left*). Three-dimensional (periodic) Voronoï tessellation with 150 grains (*right*)

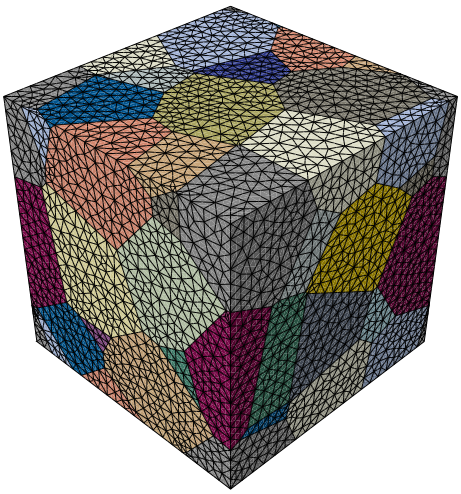

Fig. 3 Finite element representation of a volume element for polycrystalline Hastelloy X with random crystallographic orientation of the grains (using tetrahedral elements with quadratic basis functions, denoted as C3D10)

material models [10,25,53]. Convergence for the discretization could be achieved for the realizations consisting of 150 grains with 820 elements per grain.

Using this RVE, the crystal plasticity model parameters for Hastelloy X are calibrated. The model parameters are estimated through comparison of a simulated uniaxial stress–strain curve and experimental results at room temperature under quasi-static monotonic loading (Fig. 4, right) [1]. A summary of the identified model parameters is listed in Table 3. In order to take into account, the increasing influence of the strain rate at elevated temperatures, a relatively high value for m is used.

3 Simulation setup

The structure of real honeycomb seals as used in gas turbines occupies 12 % of the available space. This value is also utilized in this contribution. Figure 5, left, gives a schematic top view of the periodic honeycomb structure. The entire structure is made up by repetition of the unit cell, which is highlighted shaded in the dashed rectangle (space $\mathscr{X}$ of the unit cell with boundary $\Gamma_{\mathscr{X}}$). Throughout the simulations, only this characteristic unit cell is assumed to be relevant for determination of the overall rubbing behavior under combined thermo-mechanical loading. The selected unit cell also facilitates the application of PBC. The thickness t and the width l of the cell walls are 0.075 mm and 0.920 mm, respectively. For a regular hexagonal honeycomb structure θ is 60°. The size of the unit cell section is specified by the parameters $\Delta x = 1.6$ mm, $\Delta y = 2.772$ mm and $\Delta z = 2.0$ mm.

In Fig. 5, center two different loading positions, referred to as large and small contact, are shown. Both positions will be investigated in this contribution, since these two contact situations are often encountered

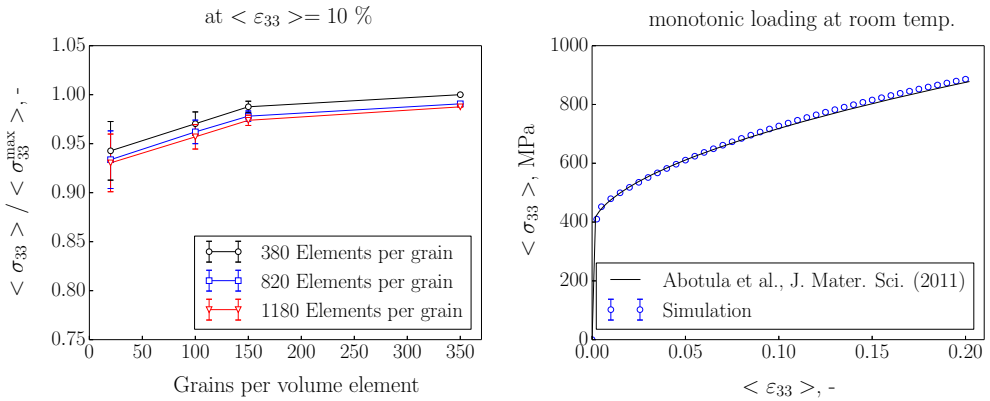

Fig. 4 Convergence study employing volume elements with different numbers of grains and finite element mesh densities (*left*). Comparison of a simulated uniaxial stress–strain curve and experimental results [1] (*right*)

Table 3 Summary of the identified crystal plasticity model parameters for Hastelloy X at room temperature

$\dot{\gamma}_0$, s^{-1}	Q_0, kJ·mol^{-1}	m, -	a, -	h_0, MPa	$\tau_{c/s,0}$, MPa	$K_{c/s}$, MPa$\sqrt{\text{mm}}$
1.6×10^{18}	119 [40]	75	1.75	1000	175/350	23.90/47.80 [19,40]

during actual rubbing. The thermo-mechanical loads emerging from the rubbing contact are schematically sketched in the far right of Fig. 5, right. The parameter $s = 0.4$ mm defines the contact width and refers to the rotating component, which is assumed to be perfectly aligned with the x-direction. All loads are located on the highlighted area of the top face of the honeycomb structure. For the thermo-mechanical analysis, first a uniform heat flux $\dot{q}$ is applied to the model as a thermal load. Afterward, this load is combined with the mechanical loads consisting of a uniform displacement u in z-direction and a uniform shear traction (stress) τ_0. The application of a displacement is justified by the rigid behavior of the rotating component. With these specifications, we define the prescribed macroscopic out-of-plane (engineering) normal strain

$$|\varepsilon_{33}^{(\text{eng})}| = \frac{< u_3 >^{z=\Delta z} - < u_3 >^{z=0}}{\Delta z}, \tag{8}$$

where $< u_3 >^{z=\Delta z}$ is the average displacement component in z-direction of the highlighted area of the top face. For the entire bottom face, it is assumed that no displacement occurs in the z-direction $\left(< u_3 >^{z=0} = 0\right)$. In the same way, the macroscopic out-of-plane (engineering) normal stress results as $|\sigma_{33}^{(\text{eng})}| = N_3/A_{0,1/s}$ (total normal force N_3 acting on the top face divided by the initial area of the large/small contact $A_{0,1/s}$). This stress can be interpreted as the mean normal stress acting in z-direction. To mimic an infinitely extended honeycomb structure in the in-plane direction, PBCs are prescribed for the nodes at the boundaries. In the initial stress-free state, the model has an homogeneous temperature distribution with initial temperature T_0. The end of the simulation is set by the time t_0. The corresponding load-time functions are also drawn in Fig. 5, right, and are derived from experimental observations.

The finite element representation of the honeycomb structure is based on the embedded cell approach consisting of a core part with a discrete microstructure and an outer macroscopic part (Fig. 6, left). While the crystal plasticity material model is assumed for the core part, the classical J_2 plasticity material model is chosen for the outer part. The microstructure is made up of polyhedric grains derived from three-dimensional Voronoï tessellations [35]. Preliminary investigations showed that a quarter of the total honeycomb structure height $\Delta z/4$ is sufficient for the core part height to accurately predict the micromechanical fields in the geometrically highly resolved region. In consistency to the investigation on the volume element, we use tetrahedral elements with quadratic basis functions (C3D10) for the finite element model. To study the influence of the average grain size of the honeycomb structure on the rubbing behavior, the mean grain size is varied between 50 and 174 µm (Fig. 6, top right). In accordance with experimental results, the individual grains are assigned with a random crystal lattice orientation and approximately one or two grains make up the cell wall thickness. Besides the different loading position (large and small contact) and the microstructure (average grain size), the

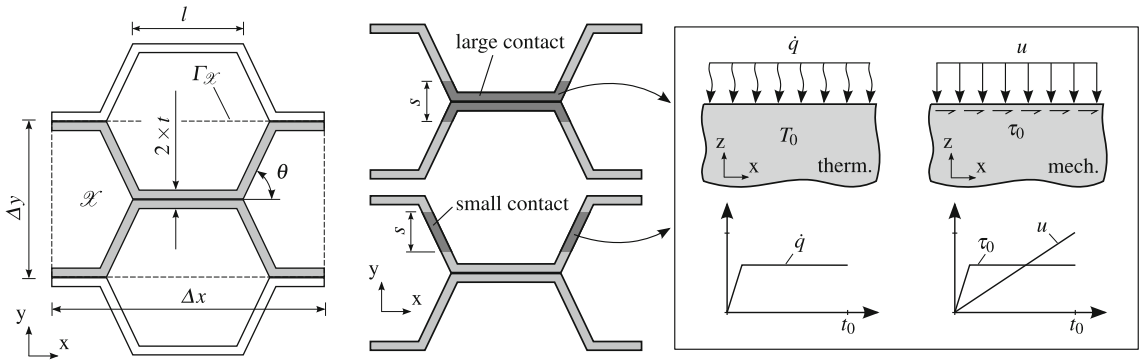

Fig. 5 Schematic representation of the hexagonal honeycomb structure with a gray-shaded region highlighting the (periodic) unit cell of the structure (*left*). Loading positions (large and small contact) with the applied thermo-mechanical loading on the top face of the (periodic) unit cell of the honeycomb structure (*center and right*)

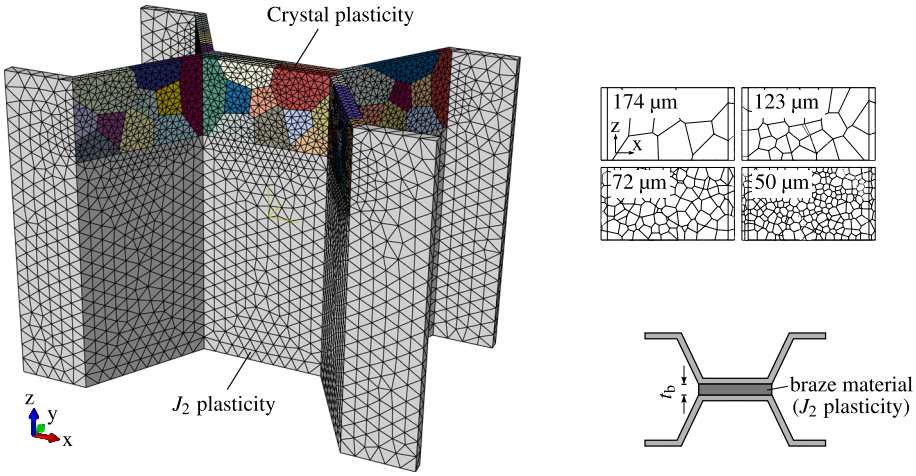

Fig. 6 Finite element model of the (periodic) unit cell of the honeycomb structure with a core part representing a discrete microstructure embedded in a macroscopic model (*left*). Four realizations of the microstructure of the honeycomb structure with different average grain size are considered in the simulation (*top right*). Schematic representation of the additional braze material between the honeycomb cell walls (*bottom right*)

influence of an additional braze material between the cell walls will be examined in this contribution (Fig. 6, bottom right). So far, it was assumed that the cell walls are perfectly joined together in the large contact situation. However, in the real manufacturing process, additional material is present between the cell walls due to capillarity effects during brazing of the honeycomb structure to its carrier plate. This additional braze material can thus significantly increase the contact area. As a first approach, the same J_2 plasticity model is assumed for the braze material as for the cell wall base material. This restricts our investigation solely to the geometric aspect of the braze material. From microstructural analysis, the thickness of the braze material t_b is roughly equal to the wall thickness of the base material ($t_\mathrm{b} = t = 0.075$ mm). The thermal effect of the brazing also results in considerable grain growth in the cell wall material. This influence is captured in the investigations using the different microstructures mentioned above.

4 Results and discussion

In this section, we examine the influence of the loading position, the average grain size and the braze material on the rubbing behavior of the polycrystalline alloy Hastelloy X. Both the thermal and mechanical responses of the honeycomb structure to rubbing are analyzed.

First, we study the influence of the two loading positions (large and small contact). In Fig. 7, left the temperature history within the respective contact areas ($z = \Delta z$) is evaluated. The maximum temperature predicted is normalized by the initial temperature. For reference, the melting temperature of the material

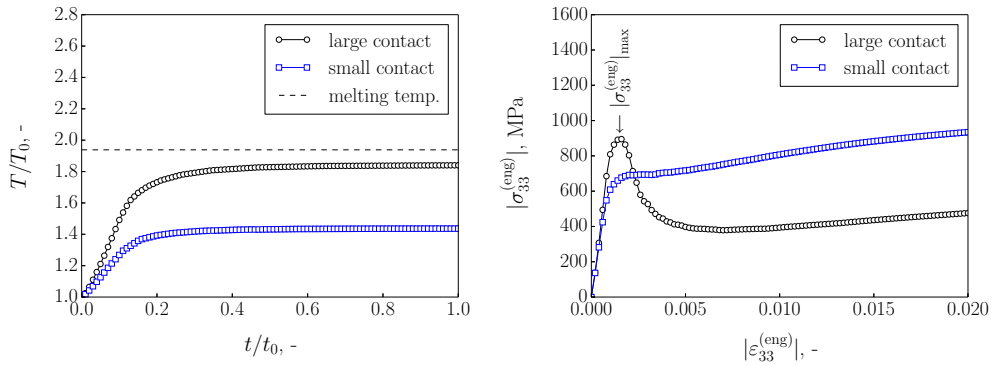

Fig. 7 Influence of the loading position (large vs. small contact) on the normalized temperature–time curve (*left*) and stress–strain curve (*right*)

is indicated. After the initial heating, which results in a highly inhomogeneous temperature distribution, both curves show a saturation behavior with respect to temperature. The large contact is clearly at a higher temperature level than the small contact. This can be attributed to the approximately 60 % larger contact area. In general, elevated temperatures should be avoided because some of the heat is expected to be transferred to the rotating component, where it can cause critical damage of its material (e.g., cracks or grain growth). In Fig. 7, right, the corresponding stress–strain curves are shown. In the initial loading phase, the large contact shows a characteristic peak value of the out-of-plane normal stress. This stress value is marked as $|\sigma_{33}^{(eng)}|_{max}$ and is assumed to significantly influence the damage behavior of the material of the rotating component. An ideal rubbing behavior is achieved at low stresses. After the characteristic peak stress, a strong decrease in the stress occurs. This is a consequence of the marked thermal softening of the material at elevated temperatures. After the strong decrease, the stress is almost saturated. In contrast, the small contact does not show a pronounced peak stress. Instead, there is a slight increase in the stress, which is caused by the compressive loading of the cell walls of the honeycomb structure. In a real rubbing process such an increase is not expected, as this additional material is likely to be rubbed away from the top face of the honeycomb structure. Then, a constant stress can be assumed.

Second, we study the influence of the average grain size. Figure 8, left, refers to the peak stresses (at $|\varepsilon_{33}^{(eng)}| = 0.0014$ %) as a function of the grain size for the large contact situation. In addition, these stresses are normalized by the maximum stress occurring for all realizations. It is apparent, that the peak stress decreases with increasing grain size. This can be attributed to the grain size effect implemented in the crystal plasticity material model. Therefore, a coarse grain structure seems to be more favorable for the rubbing behavior of the honeycomb structure. Furthermore, a coarse grain structure is known to have a positive effect on the creep properties of the material, which is relevant for this type of application. A field plot of the von Mises stress $\sigma_{v,Mis}$ at the contact time at which the peak stress occurs is shown in Fig. 8, right (large contact with an average grain size of 71 µm). One half of the core part of the honeycomb structure is shown, and the inhomogeneous stress distribution due to the random crystal lattice orientations becomes apparent. Maximum stresses occur on the sides of the large contact area. The thin cell walls at this location can be made responsible for these pronounced stresses. The highest calculated stress is 1036 MPa, which is above the ultimate tensile strength of 755 MPa at room temperature for Hastelloy X [19]. Thus, it is assumed that damage/cracking of the honeycomb structure originates at these locations.

Last, we investigate the influence of the additional braze material, see Fig. 9 (large contact with an average grain size of 71 µm). The temperature history reveals that the temperature level increases due to the additional material, as the contact area becomes larger (Fig. 9, left). The stress–strain response in case of the additional braze material shows that similar to the previous findings, a curve of characteristic peak stress, strong (thermal) softening and subsequent saturation behavior is obtained (Fig. 9, right). However, it is clear that the peak stress has also increased further (by approximately 30 %). Considering that the width of the braze material can even be greater than was assumed in the current investigations, it is essential to pay careful attention to this aspect during manufacturing of the honeycomb seals. In addition to the large contact area of this position and the fine-grained microstructure, the additional braze material can hence also be identified as a damage promoting ingredient.

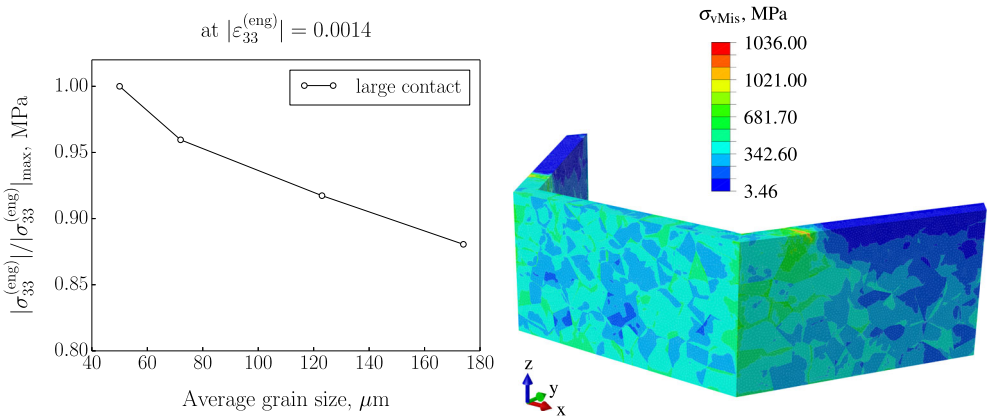

Fig. 8 Influence of average grain size on the normalized max. stress (*left*) and field plot of the von Mises stress $\sigma_{v,Mis}$ at the contact time at which the peak stress occurs (large contact with an average grain size of 71 µm) (*right*)

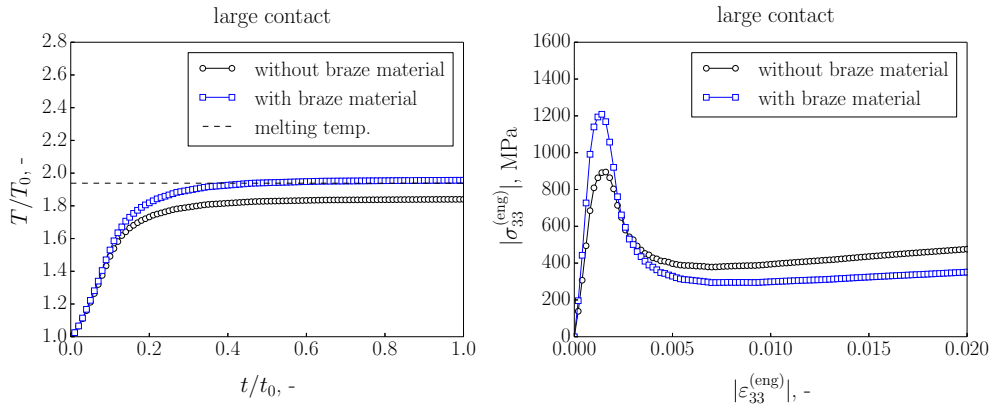

Fig. 9 Influence of the additional braze material on the normalized temperature–time curve (*left*) and stress–strain curve (*right*)

5 Conclusions

A crystal plasticity material model is set up to investigate the plastic deformation of the polycrystalline Ni-base superalloy (Hastelloy X) honeycomb structures under combined thermo-mechanical loading. The thermo-mechanical loading arises from the rubbing contact between the rotating and the stationary components of gas turbines. Even under these extreme conditions, both components should be able to operate reliably.

The predicted numerical results, based on three-dimensional finite element rubbing simulations considering microstructural features, highlight the importance of three factors influencing the failure behavior of the honeycomb structure. A large contact area, a small grain size and in particular an additional material between the cell walls seem to be key ingredients of the failure behavior. The results also reveal the importance of local field quantities, such as the local heterogeneous stress distribution, if one aims at the identification of the exact location of failure of the honeycomb structure subjected to thermo-mechanical loading occurring during rubbing. A detailed failure analysis is the topic of ongoing research.

Acknowledgements This work is part of the research project WE 2351/14–1, funded by the DFG (Deutsche Forschungsgemeinschaft). We thank the Max Planck Institut für Eisenforschung in Düsseldorf for providing the simulation kit DAMASK.

References

1. Abotula, S., Shukla, A., Chona, R.: Dynamic constitutive behavior of Hastelloy X under thermo-mechanical loads. J. Mater. Sci. **46**(14), 4971–4979 (2011)
2. Aghaie-Khafri, M., Golarzi, N.: Dynamic and metadynamic recrystallization of Hastelloy X superalloy. J. Mater. Sci. **43**(10), 3717–3724 (2008)

3. Aghaie-Khafri, M., Golarzi, N.: Forming behavior and workability of Hastelloy X superalloy during hot deformation. Mater. Sci. Eng. A **486**, 641–647 (2008)
4. Barba, D., Alabort, E., Garcia-Gonzalez, D., Moverare, J., Reed, R., Jerusalem, A.: A thermodynamically consistent constitutive model for diffusion-assisted plasticity in Ni-based superalloys. Int. J. Plast. **105**, 74–98 (2018)
5. Böhm, H.: A short introduction to basic aspects of continuum micromechanics. ILSB Report, Vienna University of Technology **206** (1998)
6. Canistraro, H.A., Jordan, E.H., Shixiang, S., Favrow, L.H., Reed, F.A.: Elastic constants of single crystal Hastelloy X at elevated temperatures. J. Eng. Mater. Technol. **120**(3), 242–247 (1998)
7. Dassault Systèmes: Abaqus 6.13 Analysis User's Guide (2013)
8. Dick, T., Cailletaud, G.: Fretting modelling with a crystal plasticity model of Ti6Al4V. Comput. Mater. Sci. **38**(1), 113–125 (2006)
9. Farukh, F., Zhao, L., Jiang, R., Reed, P., Proprentner, D., Shollock, B.: Realistic microstructure-based modelling of cyclic deformation and crack growth using crystal plasticity. Comput. Mater. Sci. **111**, 395–405 (2016)
10. Fillafer, A., Krempaszky, C., Werner, E.: On strain partitioning and micro-damage behavior of dual-phase steels. Mater. Sci. Eng. A **614**, 180–192 (2014)
11. Frederick, C., Armstrong, P.: A mathematical representation of the multiaxial bauschinger effect. G.E.G.B. Report RD/B/N **731** (1966)
12. Fritzen, F., Böhlke, T., Schnack, E.: Periodic three-dimensional mesh generation for crystalline aggregates based on Voronoi tessellations. Comput. Mech. **43**, 701–713 (2009)
13. Fromm, B.S., Chang, K., McDowell, D.L., Chen, L.Q., Garmestani, H.: Linking phase-field and finite-element modeling for process-structure-property relations of a Ni-base superalloy. Acta Mater. **60**, 5984–5999 (2012)
14. Ghosh, S., Weber, G., Keshavarz, S.: Multiscale modeling of polycrystalline nickel-based superalloys accounting for subgrain microstructures. Mech. Res. Commun. **78**, 34–46 (2016)
15. Goh, C.H., McDowell, D.L., Neu, R.W.: Characteristics of plastic deformation field in polycrystalline fretting contacts. Int. J. Fatigue **25**(9–11), 1047–1058 (2003)
16. Goh, C.H., McDowell, D.L., Neu, R.W.: Influence of microstructure in partial-slip fretting contacts based upon two-dimensional crystal plasticity simulations. J. Tribol. **128**(4), 735–744 (2006)
17. Goh, C.H., McDowell, D.L., Neu, R.W.: Plasticity in polycrystalline fretting fatigue contacts. J. Mech. Phys. Solids **54**(2), 340–367 (2006)
18. Goh, C.H., Neu, R.W., McDowell, D.L.: Crystallographic plasticity in fretting of Ti–6AL–4V. Int. J. Plast. **19**(10), 1627–1650 (2003)
19. Haynes International, I.: Hastelloy X alloy (UNS N06002). High-temperature alloys (1997)
20. Hennessey, C., Castelluccio, G.M., McDowell, D.L.: Sensitivity of polycrystal plasticity to slip system kinematic hardening laws for Al 7075–T6. Mater. Sci. Eng. A **687**, 241–248 (2017)
21. Jordan, E.H., Shi, S., Walker, K.P.: The viscoplastic behavior of Hastelloy-X single crystal. Int. J. Plast. **9**(1), 119–139 (1993)
22. Keshavarz, S., Ghosh, S.: Multi-scale crystal plasticity finite element model approach to modeling nickel-based superalloys. Acta Mater. **61**, 6549–6561 (2013)
23. Kouznetsova, V.: Computational homogenization for the multi-scale analysis of multi-phase materials. Ph.D. thesis, TU Eindhoven (2002)
24. Kumar, R., Wang, A., McDowell, D.L.: Effects of microstructure variability on intrinsic fatigue resistance of nickel-base superalloys - a computational micromechanics approach. Int. J. Fract. **137**, 173–210 (2006)
25. Lin, B., Zhao, L., Tong, J., Christ, H.: Crystal plasticity modeling of cyclic deformation for a polycrystalline nickel-based superalloy at high temperature. Mater. Sci. Eng. A **527**(15), 3581–3587 (2010)
26. Meier, F.: Influence of the aluminum-microstructure on the damage behavior of integrated circuits. Ph.D. thesis, Technical University of Munich (2017)
27. Meier, F., Schwarz, C., Werner, E.: Crystal-plasticity based thermo-mechanical modeling of Al-components in integrated circuits. Comput. Mater. Sci. **94**, 122–131 (2014)
28. Mohr, D.: Multi-scale finite-strain plasticity model for stable metallic honeycombs incorporating microstructural evolution. Int. J. Plast. **22**, 1899–1923 (2006)
29. Mohr, D., Doyoyo, M.: Deformation-induced folding systems in thin-walled monolithic hexagonal metallic honeycomb. Int. J. Solids Struct. **41**, 3353–3377 (2004)
30. Mohr, D., Doyoyo, M.: Large plastic deformation of metallic honeycomb: orthotropic rate-independent constitutive model. Int. J. Solids Struct. **41**, 4435–4456 (2004)
31. Musinski, W.D., McDowell, D.L.: Microstructure-sensitive probabilistic modeling of HCF crack initiation and early crack growth in Ni-base superalloy IN100 notched components. Int. J. Fatigue **37**, 41–53 (2011)
32. Musinski, W.D., McDowell, D.L.: On the eigenstrain application of shot-peened residual stresses within a crystal plasticity framework: Application to Ni-base superalloy specimens. Int. J. Mech. Sci. **100**, 195–208 (2015)
33. Nygards, M., Gudmundson, P.: Three-dimensional periodic Voronoi grain models and micromechanical FE-simulations of a two-phase steel. Comput. Mater. Sci. **24**, 513–519 (2002)
34. Przybyla, C.P., McDowell, D.L.: Microstructure-sensitive extreme value probabilities for high cycle fatigue of Ni-base superalloy IN100. Int. J. Plast. **26**, 372–394 (26)
35. Quey, R., Dawson, P., Barbe, F.: Large-scale 3D random polycrystals for the finite element method: generation, meshing and remeshing. Comput. Methods Appl. Mech. Eng. **200**, 1729–1745 (2011)
36. Roters, F., Diehl, M., Shanthraj, P., Eisenlohr, P., Reuber, C., L.Wong, S., Ma, D., Jia, N., Kok, P., Fujita, N., Ebrahimi, A., Hochrainer, T., Grilli, N., Janssens, K., Stricker, M., Weygand, D., Meier, F., Werner, E., Fabritius, H.O., Nikolov, S., Friak, M., Raabe, D.: Damask - the Düsseldorf advanced material simulation kit for modelling multi-physics crystal plasticity, damage and thermal phenomena from the single crystal up to the component scale. Comput. Mater. Sci. (**in press**) (2018)

37. Roters, F., Eisenlohr, P., Hantcherli, L., Tjahjanto, D., Bieler, T., Raabe, D.: Overview of constitutive laws, kinematics, homogenization and multiscale methods in crystal plasticity finite-element modeling: therory, experiments, applications. Acta Mater. **58**(4), 1152–1211 (2010)
38. Roters, F., Eisenlohr, P., Kords, C., Tjahjanto, D., Diehl, M., Raabe, D.: Damask: The Düsseldorf advanced material simulation kit for studying crystal plasticity using an FE based or a spectral numerical solver. Procedia IUTAM **3**, 3–10 (2012)
39. Rycroft, C.H.: Voro++: a three-dimensional Voronoi cell library in C++. Chaos **19**, 041–111 (2009)
40. Sakthivel, T., Laha, K., Nandagopal, M., Chandravathi, K.S., Parameswaran, P., Selvi, S.P., Mathew, M., Mannan, S.K.: Effect of temperature and strain rate on serrated flow behaviour of Hastelloy X. Mater. Sci. Eng. A **534**, 580–587 (2012)
41. Shahba, A., Ghosh, S.: Crystal plasticity FE modeling of Ti alloys for a range of strain-rates. Part I: a unified constitutive model and flow rule. Int. J. Plast. **87**, 48–68 (2016)
42. Shenoy, M.M., Gordon, A.P., McDowell, D.L., Neu, R.W.: Thermomechanical fatigue behavior of a directionally solidified Ni-base superalloy. J. Eng. Mater. Technol. **127**, 325–336 (2005)
43. Shi, S., Jordan, E.H., Walker, K.P.: Self-consistent constitutive modeling and testing of polycrystalline Hastelloy-X. Int. J. Solids Struct. **29**(21), 2623–2638 (1992)
44. Song, J.E., McDowell, D.L.: Grain scale crystal plasticity model with slip and microtwinning for a third generation Ni-base disk alloy. Superalloys **2012**, 159–166 (2012)
45. Taxer, T., Schwarz, C., Smarsly, W., Werner, E.: A finite element approach to study the influence of cast pores on the mechanical properties of the Ni-base alloy MAR-M247. Mater. Sci. Eng. A **575**, 144–151 (2013)
46. Varshni, Y.P.: Temperature dependence of the elastic constants. Phys. Rev. B **2**(10), 3952–3958 (1970)
47. Wang, A., McDowell, D.L.: Yield surfaces of various periodic metal honeycombs at intermediate relative density. Int. J. Plast. **21**(2), 285–320 (2005)
48. Werner, E., Wesenjak, R., Fillafer, A., Meier, F., Krempaszky, C.: Microstructure-based modelling of multiphase materials and complex structures. Contin. Mech. Thermodyn. **28**(5), 1325–1346 (2015)
49. Ye, C., Chen, J., Xu, M., Wei, X., Lu, H.: Multi-scale simulation of nanoindentation on cast Inconel 718 and NbC precipitate for mechanical properties prediction. Mater. Sci. Eng. A **662**, 385–394 (2016)
50. Zhang, M., McDowell, D.L., Neu, R.W.: Microstructure sensitivity of fretting fatigue based on computational crystal plasticity. Tribol. Int. **42**, 1286–1296 (2009)
51. Zhang, M., Neu, R.W., McDowell, D.L.: Microstructure-sensitive modeling: application to fretting contacts. Int. J. Fatigue **31**, 1397–1406 (2009)
52. Zhang, T., Jiang, J., Britton, B., Shollock, B., Dunne, F.: Crack nucleation using combined crystal plasticity modelling, high-resolution digital image correlation and high-resolution electron backscatter diffraction in a superalloy containing non-metallic inclusions under fatigue. Proc. Math. Phys. Eng. Sci. **472**, 1–25 (2016)
53. Zhang, X., Oskay, C.: Polycrystal plasticity modeling of nickel-based superalloy IN 617 subjected to cyclic loading at high temperature. Modell. Simul. Mater. Sci. Eng. **24**, 1–27 (2016)